# NUMERICAL INVESTIGATION OF THE FLOW FIELD IN A HIGH-ASPECT-RATIO COOLING DUCT

**T. Kaller[1], V. Pasquariello[2], S. Hickel[3] and N.A. Adams[4]**

[1,2,4] Technical University of Munich
Department of Mechanical Engineering
Chair of Aerodynamics and Fluid Mechanics
Boltzmannstr. 15, 85748 Garching bei München, Germany

[3] Faculty of Aerospace Engineering, Technische Universiteit Delft
P.O. Box 5058, 2600 GB Delft, The Netherlands

## ABSTRACT

We present well-resolved large-eddy-simulations (LES) of a straight, high-aspect-ratio cooling duct (HARCD) at a bulk Reynolds number of $Re = 110 \cdot 10^3$ and an average Nusselt number of $Nu = 371$. The geometry and boundary conditions have been defined in cooperation with [1], who conducted the experimental measurements for this case. As coolant subcritical water was chosen. The current investigation focuses on the influence of asymmetrical wall heating on the flow field and specifically on the influence of the turbulence-induced secondary flow on turbulent heat transfer, the spatial development of the temperature boundary layer along the duct length and the accompanying viscosity modulation. Due to the viscosity drop in the vicinity of the heated wall we observe a decrease in turbulent length scales and in turbulence anisotropy, resulting in a decrease of turbulent mixing and the secondary flow strength along the duct.

## 1. INTRODUCTION

The turbulent flow and heat transfer in a high-aspect-ratio ($AR$) duct with rectangular cross section is of great interest for many engineering applications. Examples range from cooling ducts in motors of hybrid electrical vehicles over ventilation systems to the cooling systems of rocket engines. For the ability to predict the cooling efficiency and therefore the lifetime of the respective technical system a profound understanding of cooling duct flows is required.

The turbulent flow through a straight rectangular duct is strongly influenced by the turbulence-induced secondary flow, the so called Prandtl's flow of the second kind. In each of the four duct corners, a pair of counter-rotating streamwise vortices forms as a consequence of the anisotropy of the Reynolds stress tensor. These are therefore not present in simulations using a Reynolds-averaged Navier-Stokes (RANS) model based on the isotropic turbulence assumption. The secondary flow is relatively weak, $1-3\%$ of the bulk velocity, however it has a significant influence on momentum and temperature transport and increases the mixing between hot and cold fluid.

Several experimental and numerical studies investigated duct flows of different cross-section. [2], [3]and [4] conducted first experiments of air flow through adiabatic square ducts with a special focus on secondary flows. The influence of wall heating was analyzed by [5] for a channel flow. [6] studied the flow through an adiabatic high-aspect-ratio duct with $AR = 11.7$. [7] performed a first LES of a periodic heated square duct and studied the influence of wall heating on the flow field. [8] extended this work to investigate the spatial development of the temperature boundary layer. [9] analyzed the turbulent heat transfer for rectangular ducts with moderate aspect ratios ranging from $AR = 0.25$ to $AR = 1.5$. [10] performed a direct numerical simulation (DNS) of a square duct in order to investigate the generation of the secondary flow. [11] presented DNS simulations of adiabatic periodic duct flows for various aspect ratios ranging from $AR = 1$ to $AR = 7$. All the numerical studies have been conducted at a much lower Reynolds-number than the present study.

In this work, we investigate the influence of asymmetric wall heating on an $AR = 4.3$ duct at a Reynolds-number of $110 \cdot 10^3$ with a moderate temperature difference between coolant and heated wall via LES. We also present a comparison of experimental PIV and the LES results. The main focus of the LES study lies on the effect of wall heating on the turbulence, the secondary flow field and the temperature boundary layer growth along the duct length.

## 2. NUMERICAL MODEL

For our present study using liquid water as coolant only small density variations are present. The flow is described by the incompressible Navier-Stokes equations and the Boussinesq approximation for the gravitational force term. The temperature is treated as an active scalar. The thermodynamic properties of the fluid, which are a function of temperature and density, are obtained using the IAPWS correlations, see [12].

The transport equations are discretized by a fractional step finite-volume method on a block structured, staggered Cartesian grid. As time advancement method an explicit third-order Runge-Kutta scheme by [13] is applied, while the time-step is adjusted dynamically to maintain a maximum Courant number of 1.0.

For discretizing the pressure Poisson equation and the diffusive fluxes, second-order accurate central difference schemes are implemented. The pressure Poisson equation is solved in every Runge-Kutta substep using a Krylov subspace solver with an algebraic-multigrid (AMG) preconditioner for convergence acceleration. For discretization of the convective fluxes, the Adaptive Local Deconvolution Method (ALDM) is used, respectively the computationally more efficient simplified SALD method. ALDM is a nonlinear finite volume method that provides a physically consistent subgrid-scale turbulence model for implicit LES, see [14] and [15]. For the extension and validation for the Boussinesq equations see [16].

## 3. SIMULATION SETUP

The experimental setup of the water cooling duct is defined as follows. First water at a bulk temperature of $T_b = 333.15\,\mathrm{K}$ is pumped with a constant flow rate of 50 l/min from a reservoir into a 600 mm unheated feed line. This flow rate corresponds to a bulk

[1] thomas.kaller@tum.de
[2] vito.pasquariello@tum.de
[3] s.hickel@tudelft.nl
[4] nikolaus.adams@tum.de

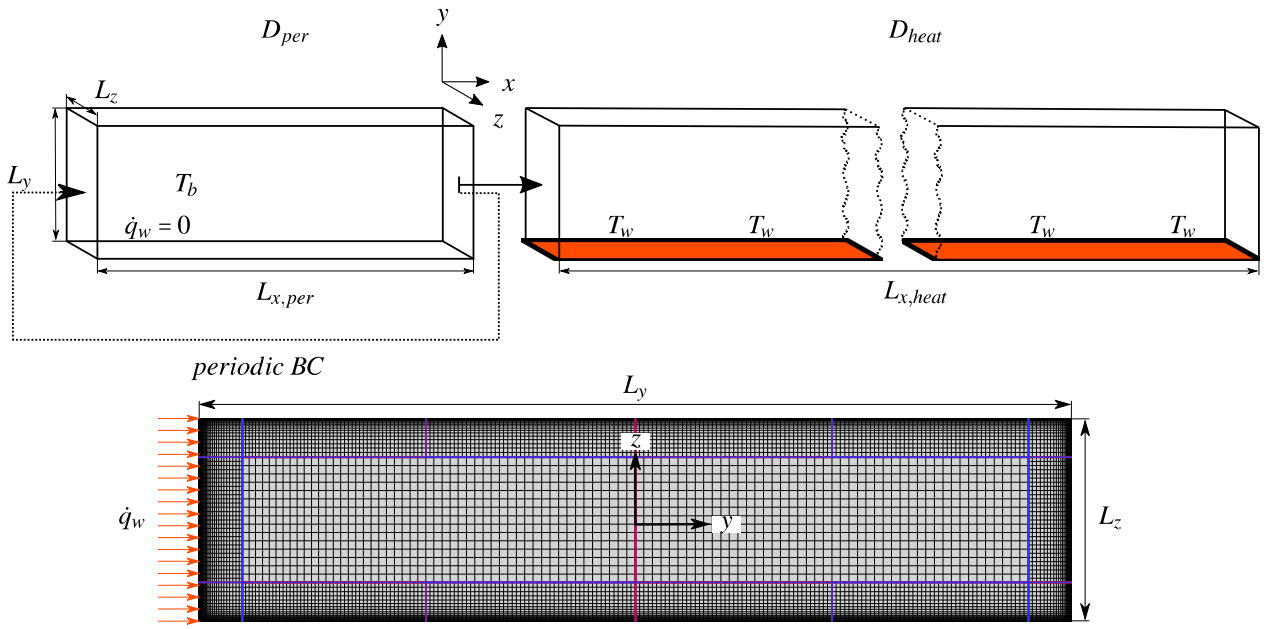


Figure 1: Sketch of the numerical cooling duct setup with periodic domain $D_{per}$ and spatially resolved heated domain $D_{heat}$. At the bottom the computational grid and blocking in the $yz$-plane is depicted (every 2nd grid line shown).

flow velocity of $u_b = 5.38$ m/s. After a flow straigthener the fluid enters into the heated test section of equally 600 mm, where a constant wall temperature of $T_w = 373.15\,\mathrm{K}$ is applied at the lower wall. Both sections are straight ducts of equal cross-section. For further details we refer to [1].

Figure 1 depicts the numerical setup consisting of the adiabatic periodic domain and the heated domain denoted by $D_{per}$ and $D_{heat}$ respectively. The feed line is modeled as a short periodic duct piece and serves as turbulent inflow generator for the heated duct. For each time-step, the outflow velocity profile of $D_{per}$ is prescribed at the inlet of $D_{heat}$. At the end of the heated duct, a second-order Neumann boundary condition is applied for velocity and density fluctuations and for the pressure a Dirichlet boundary condition is set.

The duct has a nominal height of $L_y = 25.8$ mm and a width of $L_z = 6$ mm, which results in an aspect ratio of $AR = 4.3$ and a hydraulic diameter of $d_h = 9.74$ mm. The streamwise length of $D_{per}$ is chosen to $L_{x,per} = 7.5 \cdot d_h$ to resolve the large-scale turbulent structures following [11]. The heated duct is spatially fully represented with a length of $L_{x,heat} = 600$ mm, corresponding to $61.6\,d_h$. All walls are defined as smooth adiabatic walls except the lower wall of the heated duct section, where the constant temperature $T_w$ is prescribed.

To generate the initial solution for the combined setup of $D_{per}$ and $D_{heat}$ we use several steps. First the velocity profile for a fully developed laminar duct flow superimposed with white noise of amplitude $A \approx 5\%\,u_b$ is defined on a coarse grid variant of the adiabatic duct $D_{per}$. After the state of a fully developed turbulent duct flow is reached, the solution is interpolated onto the fine grid and the simulation continued for several flow-through times (FTT). The final flow state of $D_{per}$ forms the initial condition for the full coupled setup of both flow domains, where $D_{heat}$ is built as a sequence of periodic duct sections. The heating is switched on by setting the isothermal wall temperature to $T_w = 373.15\,\mathrm{K}$ at the lower wall. After 1.33 FTT with respect to $L_{x,heat}$ and $u_b$, statistical sampling is started with a constant temporal sampling interval of $\Delta t_{sample} = 0.025 \cdot (d_h/u_b)$. The sampling then extends over 20 FTT. The main flow and simulation parameters are listed in table 1. All Reynolds-numbers are formed using $d_h$ as reference length. The friction Reynolds-numbers are measured in the center of their respective sidewall and represent the adiabatic case. When heating is applied to the lower wall, $Re_{\tau,y}$ increases from the 5500 of the adiabatic case to 7300. The Prandtl-number is a function of local temperature and at bulk conditions $Pr_b = 3$. The Nusselt-number represents the mean value for the whole domain $D_{heat}$.

Table 1: Main flow and simulation parameters.

| $Re$ | $Nu$ | $Re_{\tau,y}$ | $Re_{\tau,z}$ | $T_b\,[\mathrm{K}]$ | $T_w\,[\mathrm{K}]$ |
|---|---|---|---|---|---|
| $110 \cdot 10^3$ | 371 | 4800 | 5500 | 333.15 | 373.15 |

An extensive grid sensitivity analysis has been performed for the adiabatic duct in order to determine the required grid resolution for a well-resolved LES. Because we use a matching interface, the same mesh is applied for $D_{per}$ and $D_{heat}$. As depicted in figure 1 we apply a 2:1 connection at the interface of wall blocks and the two inner blocks to reduce the computational cost. All blocks have a uniform discretization in streamwise direction and the boundary layer blocks have a hyperbolic grid stretching in their respective wall-normal direction. For $Pr > 1$ thermal length scales are smaller than the momentum length scales and the temperature boundary layer is completely contained inside the momentum boundary layer. In order to resolve the temperature gradient, the wall-normal resolution at the heated wall is increased leading to an asymmetric grid with respect to the $y-$axis.

The main grid parameters for both domains are listed in table 2, due to the aforementioned asymmetry separately for the heated lower and the adiabatic upper wall. The number of cells in each direction is denoted by $N_x$, $N_y$ and $N_z$. In total $\approx 280 \cdot 10^6$ cells are used for the discretization of the complete configuration. The dimensionless wall distances of the first respective cell are denoted by $\Delta x^+$, $\Delta y^+_{min}$ and $\Delta z^+_{min}$ and are normalized by the in-

Table 2: Main parameters for grid shown in figure 1.

| | $D_{per}\|_{lower}$ | $D_{per}\|_{upper}$ | $D_{heat}\|_{lower}$ | $D_{heat}\|_{upper}$ |
|---|---|---|---|---|
| $N_x \times N_y \times N_z$ | $576 \times 501 \times 141$ | $576 \times 501 \times 141$ | $4740 \times 501 \times 141$ | $4740 \times 501 \times 141$ |
| $\Delta x^+ \times \Delta y^+_{min} \times \Delta z^+_{min}$ | $62.7 \times 0.73 \times 1.42$ | $62.9 \times 1.24 \times 1.42$ | $94.5 \times 1.09 \times 1.42$ | $62.8 \times 1.24 \times 1.42$ |
| $\frac{\Delta y_{max}}{\Delta y_{min}} \times \frac{\Delta z_{max}}{\Delta z_{min}}$ | $33.2 \times 27.3$ | $24.2 \times 27.3$ | $33.2 \times 27.3$ | $24.2 \times 27.3$ |

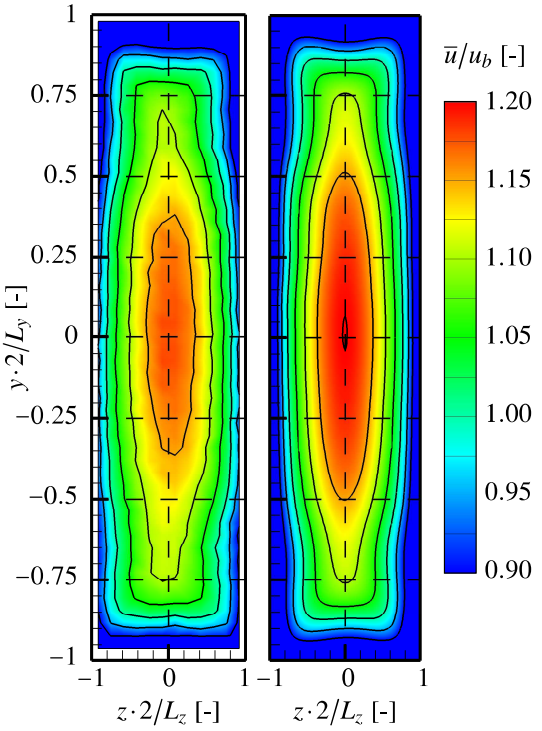


Figure 2: Comparison of streamwise velocity in the cross section of the heated duct for the experimental PTV and the numerical LES results. The heated wall is located at the lower side at $y = y_{min}$ . Due to reflections the experimental data in the vicinity of the walls is cut off.

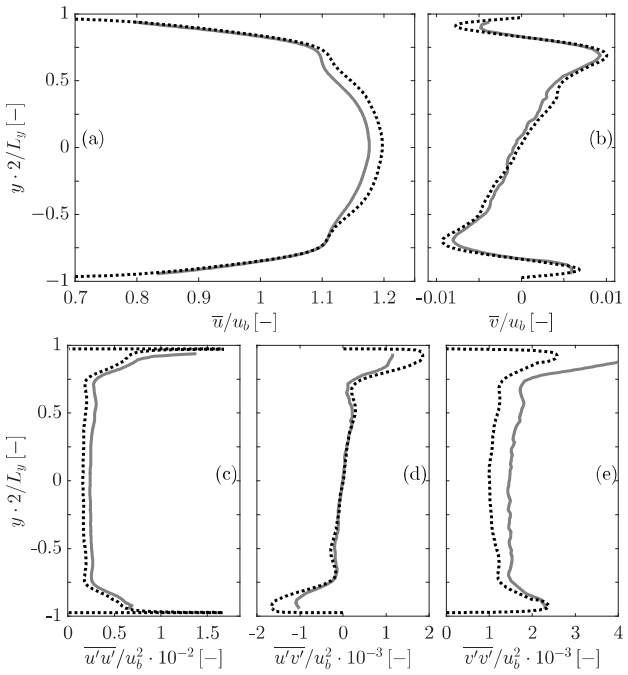


Figure 3: Comparison of experimental ( ——— ) and numerical ( ····· ) results for the heated duct. Figures (a)/(b) show the streamwise and heated wall-normal velocity respectively and figures (c)/(d)/(e) the Reynolds stress distribution along the duct center line.

ner length scale $l^+ = \nu_w/u_\tau$ with the friction velocity defined as $u_\tau = \sqrt{\tau_w/\rho_w}$. The quantities are evaluated at the respective wall center. The coarsening ratios $\frac{\Delta y_{max}}{\Delta y_{min}}$ and $\frac{\Delta z_{max}}{\Delta z_{min}}$ relate the largest cell size to the smallest cell size in the boundary layer blocks.

## 4. RESULTS

### 4.1. Validation with experimental data

The numerical LES results are compared to the experimental PIV (Particle Image Velocimetry) and the experimental PTV (Volumetric Particle Tracking Velocimetry) results. For further details on the conducted measurements we refer to [1].

We observe a good agreement between the PTV results and the LES results for the cross-sectional streamwise velocity field in figure 2. Both experimental and numerical results are spatially averaged over the field of view (FOV) ranging from 350 – 400 mm. Due to fabrication tolerances the experimental duct is on average slightly narrower than in the LES leading to a difference in the aspect ratio of $AR_{LES} = 25.8/6.0 = 4.30$ and $AR_{PIV} = 26.1/6.23 = 4.19$ respectively. Due to the slightly narrower duct of the LES we see an increase of the core velocity, which we will quantify using the PIV results.

Figure 3 shows the comparison between the LES and the PIV results. An averaging in streamwise direction over the FOV and across the laser sheet thickness of $\Delta LS = 1$ mm is performed. For the latter a constant Gaussian laser intensity distribution along the $y$-axis is assumed. To account for the different aspect ratio a scaling with respect to the $y$-axis is performed for the LES data with a factor of $AR_{PIV}/AR_{LES}$.

For the velocity profile in figure 3 (a) we observe a very good agreement. Until approximately $2y/L_y = \pm 0.75$ the streamwise velocities coincide perfectly. The shoulder section profiles from $-0.75$ to $-0.5$ agree well. At the opposite wall larger deviations are present due to an asymmetry of the experimental PIV data. As already seen in the comparison with the PTV data, the core velocity is slightly higher because of the narrower cross-section. Compared to the PIV results $\overline{u}/u_b$ is 1.71% larger in the LES. The numerical and experimental $\overline{v}$-profiles also agree very well. The peak positions, which indicate the influence of the corner vortices on the duct center, match perfectly. However, the maximum

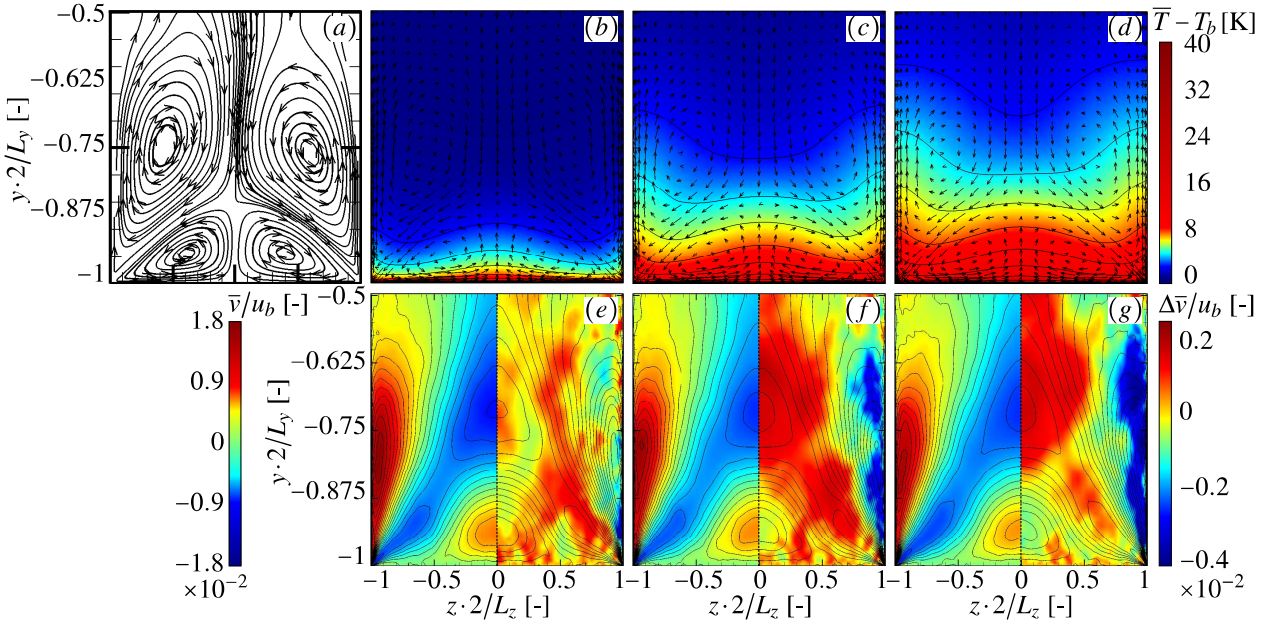


Figure 4: Development of the temperature boundary layer and accompanying change in secondary flow velocity along the duct length in the vicinity of the heated wall. Figure (a) shows the counter-rotating vortices and figures (b)/(c)/(d) the temperature increase at 100 mm, 400 mm and 600 mm respectively. Figures (e)/(f)/(g) depict on the left of the duct center the wall-normal velocity $\overline{v}$ and on the right the change in $\overline{v}$ with respect to the unheated periodic duct, $\Delta\overline{v} = \overline{v} - \overline{v}_{per}$.

values are again slightly higher. We observe a relatively large deviation for the $\overline{v}$-minimum at the $y = y_{max}$ wall, which we attribute to the aforementioned asymmetry of the experimental data.

In figure 3 (c)/(d)/(e) the comparison of the Reynolds stresses is depicted. The streamwise component $\overline{u'u'}$ shows a satisfactory agreement. Probably due to measurement noise the LES has consistently lower values than the PIV. The coarser grid in the duct core due to the 2:1 connection as source of this deviation can be ruled out as an increase of the resolution leads to the same result. The $\overline{u'v'}$ profiles match very well except in the vicinity of the walls, where the LES has higher extrema. The $\overline{v'v'}$ profiles coincide in the vicinity of the heated wall. In the duct center we observe a similar offset like that in $\overline{u'u'}$. At the upper wall large deviations are visible due to an overshoot in the experimental data.

[1] reported, that the experimental data exhibits uncertainties with respect to the laser sheet misalignment and the effective laser sheet thickness. Hence, the latter might be larger than the nominal thickness of $\Delta LS = 1$ mm, which we assumed for postprocessing the LES results. We investigated the influence on the LES data and observed, that both misalignment and an increased $\Delta LS$ lead to an improved agreement of LES and PIV.

## 4.2. The flow field of adiabatic and heated duct

In this chapter we analyze the turbulent heat transfer in the asymmetrically heated duct based on the LES results. The main focus lies on investigating the differences of the adiabatic and the heated duct flow field, i.e. on the influence of the wall heating along the duct. As a consequence of the heating, the temperature in the vicinity of the wall increases with the streamwise distance, reducing the local viscosity, which may drop up to $\nu(T_w)/\nu(T_b) = 0.62$.

The development of the temperature boundary layer is strongly influenced by the secondary flow structures. Figure 4 (a) shows the pairs of counter-rotating vortices, which form in each of the duct corners. In the lower left corner for example, the smaller counter-clockwise (CCW) rotating vortex is forming along the short sidewall and the larger clockwise (CW) rotating vortex along the large sidewall (mirror-inverted for the opposite half of the duct). Each vortex extends to the respective symmetry plane, where it meets the vortex from the opposite side. The strength of these vortices and the associated secondary flow is relatively weak. In our case, the maximum cross-flow velocity for the adiabatic duct is $\overline{u}_{cf}/u_b = \sqrt{\overline{v}^2 + \overline{w}^2}/u_b = 1.93\%$. This value lies perfectly within the $1-3\%$ range reported in the literature, see [7]. Figures 4 (b)/(c)/(d) depict the axial development of the temperature boundary layer at several streamwise locations along the heated duct. The thermal boundary layer thickness increases in streamwise direction due to conduction, turbulent mixing and through transport by the mean secondary flow. The latter is responsible for the characteristic bent shape of the temperature profile indicated by the isolines. In the left duct quarter, the CW vortex is transporting the heated fluid away from the heated wall along the large sidewall into the cooler duct core and from there cold fluid downwards along the center line. The CCW vortex conveys hot fluid from the corner along the heated wall to the heated walls center at $z = 0$ and then upwards along the midplane. There it mixes with the cold fluid transported downwards. Both vortices push the relatively cold duct core fluid into the lower left corner.

The heating and therefore the temperature increase and the accompanying viscosity decrease is relatively moderate. Still a significant weakening of the secondary flow strength can be observed in figures 4 (e)/(f)/(g), in which the secondary flow component in normal direction of the heated wall $\overline{v}$ is depicted at the same streamwise positions as the temperature boundary layer plots above. In the left quadrant of each picture the mean vertical velocity $\overline{v}$ is shown and in the right quadrant the difference of the $\overline{v}$-field with respect to the adiabatic case. Comparing $\Delta\overline{v}$, we observe a significant reduction of the vortex strength along the heated duct. The upward transport of hot fluid in the vicinity of the large sidewall is slowed down increasingly, in the end cross-section at 600 mm the maximum $\Delta\overline{v}/u_b$ is $\approx -0.004$ with a

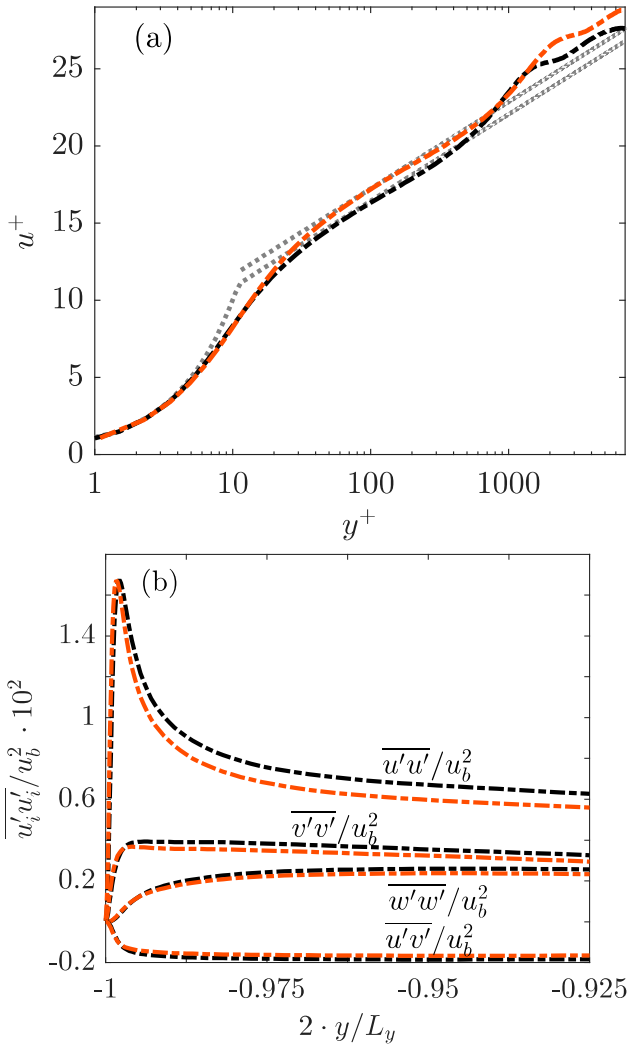


Figure 5: Profiles of (a) mean streamwise velocity and (b) Reynolds stresses along the duct height at $z = 0$ for the adiabatic ( −·−·− ) and the heated duct ( −·−·− ). The law of the wall is represented by ( ····· ).

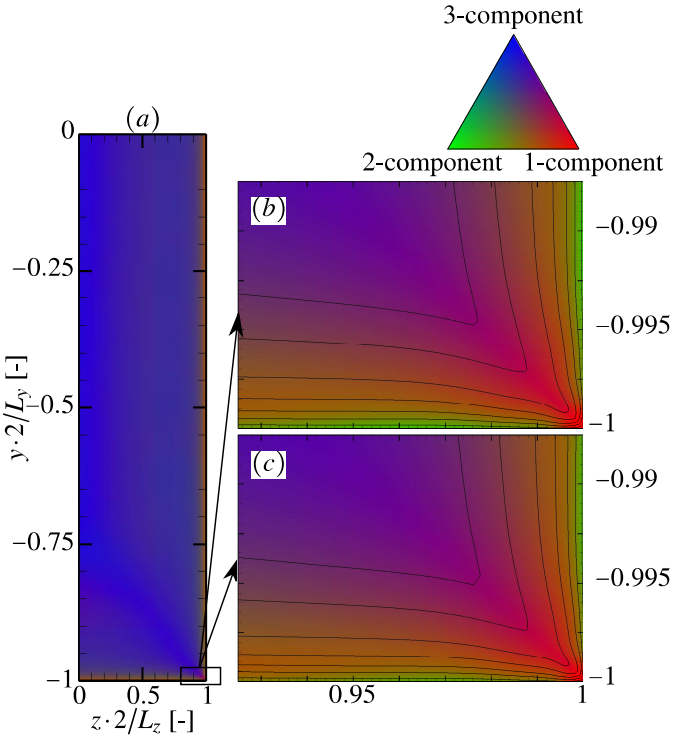


Figure 6: Barycentric anisotropy map illustrating regions of 1-, 2- and 3-component turbulence with (a) adiabatic duct, (b) zoom into the corner and (c) the same view for the heated duct. Isolines signify a constant 3-component fraction.

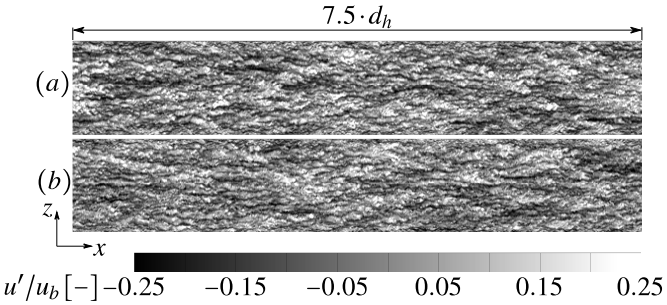


Figure 7: Streamwise velocity fluctuations at the heated wall for (a) adiabatic ($y^+ = 16.1$) and (b) heated duct ($y^+ = 24.2$). The complete streamwise length of the adiabatic duct section and the last $7.5 \cdot d_h$ of the heated duct are shown.

velocity of $\bar{v}/u_b \approx 0.015$. These values correspond to a reduction of approximately −25%. The positions of the vortices stay nearly constant and are therefore defined mainly by the duct geometry. Only for the larger vortex we observe a slight shift in the direction of both the short and the large sidewall. As the corner vortices are Reynolds stress induced, we will now further analyze the influence of the reduced wall viscosity on the turbulence field.

By comparing the adiabatic domain $D_{per}$ with $D_{heat}$ in figure 5, we investigate the influence of the wall heating on the turbulent boundary layer in the duct center at $z = 0$. A spatial averaging is applied, for $D_{per}$ over the whole length of $L_{x,per} = 7.5 d_h$ and for $D_{heat}$ over the last $7.5 d_h$ of $L_{x,heat}$ and hence assuming local homogenity. For both duct sections the law of the wall velocity profile is obtained, $u^+ = y^+$ for the viscous sublayer and $u^+ = 1/\kappa \cdot \ln y^+ + B$ for the log-law region. Analogous to [17], we observe in figure 5 (a), that the heating causes a shift in the log-law velocity profile. For our setup, the integration constant increases from $B = 5.2$ of the adiabatic to $B = 6.0$ for the heated case. The von Kármán constant and with it the velocity profiles slope remains unchanged at $\kappa = 0.41$. Figure 5 (b) depicts the change in the Reynolds stress profiles in the heated wall boundary layer. The $\overline{u'u'}$-peak shifts a bit closer to the wall, whereas the maximum value is unchanged. In accordance with [18] applying heating to the flow leads to a reduction of the turbulence intensities in all directions. This seems counterintuitive, as with lower viscosity one would expect an increase in turbulent fluctuations. This observation is indeed in agreement with previous studies of [17] and [18] showing, that the heating of the fluid and with it the drop in viscosity exhibits a stabilizing effect on the boundary layer.

The heating also affects the anisotropy of the turbulence field. A classical way to study turbulence anisotropy are anisotropy invariant maps. As an extension [19] introduced the barycentric map, which provides a more intuitive visualization technique. Its

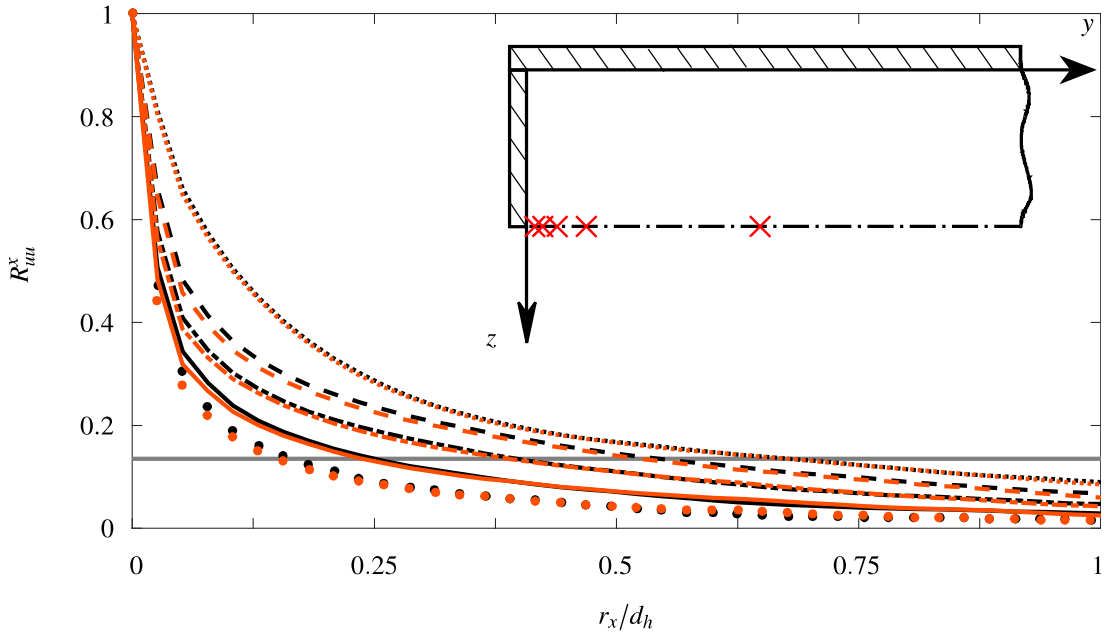


Figure 8: Streamwise autocorrelations of streamwise velocity. Black lines represent the adiabatic and orange ones the heated case. ( ● ) is taken at $y^+ = 16.1$, ( ——— ) at $y^+ = 30.1$, ( −·−·− ) at $y^+ = 60.5$, ( - - - - - - ) at $y^+ = 120.6$ and ( ····· ) at $y^+ = 627.0$. All $y^+$ values refer to the adiabatic duct.

construction is based on the eigenvalues $\lambda_i$ of the Reynolds stress tensors anisotropy tensor. The basic principle is, that any realizable turbulence state can be represented as a combination of the three limiting states of 1-, 2- and 3-component turbulence. These limiting states are set as the corners of an equilateral triangle with $\mathbf{x}_{1c} = (1,0)$, $\mathbf{x}_{2c} = (0,0)$ and $\mathbf{x}_{3c} = (1/2, \sqrt{3}/2)$. The coordinates of an arbitrary turbulent state can then be computed as $\mathbf{x} = C_{1c}\mathbf{x}_{1c} + C_{2c}\mathbf{x}_{2c} + C_{3c}\mathbf{x}_{3c}$ with the weights $C_{ic}$ deduced from the Eigenvalues $\lambda_i$. At the end we map the coefficient vector $C_{ic}$ to the RGB color triplet. The comparison of the anisotropy field in the immediate vicinity of the duct corners in figure 6 reveals, that the anisotropy in the vicinity of the heated wall is reduced, in this case the fraction of 2-component turbulence. Hence, the flow becomes more isotropic. This leads in turn to a weaker secondary flow as the anisotropy of the Reynolds stress tensor is the basis of the production term of the streamwise vorticity.

As discussed before, the viscosity reduction changes the turbulence field in the vicinity of the heated wall. We now want to analyze qualitatively and quantitatively the influence on turbulent length scales. Figure 7 shows the instantaneous streamwise velocity fluctuations in a plane parallel to the heated wall for both the adiabatic and the heated duct. For the first the complete length and for the latter the last $7.5 \cdot d_h$ section is shown. On the one hand we observe relatively small turbulent structures due to the high Reynolds-number flow and on the other hand, that hardly any difference between the heated and non-heated result is visible due to the moderate temperature difference of $\Delta T = 40K$. Figure 8 presents streamwise autocorrelation functions $R^x_{uu}$ taken in the duct center $z = 0$ at different $y$-locations in the vicinity of the heated wall. For the definition of the longitudinal correlation of the $u$-velocity we assume local homogeneity in streamwise direction over $D_{per}$ and the last $7.5\,d_h$ of the heated duct. The number of time-steps required until a converged result is reached can then be reduced by evaluating $R^x_{uu}$ as

$$(1) \quad R^x_{uu}(r_x) = R^x_{uu}(k_r \cdot \Delta x) = \frac{\sum_{i=1}^{N_x - k_r} \left( \overline{u'(x_i,t) \cdot u'(x_i + k_r \cdot \Delta x, t)} \right)}{N_x - k_r}$$

following [20] with $k_r = 0, 1, \ldots, N_x - 1$, the velocity fluctuations $u'(x_i,t) = u(x_i,t) - \overline{u}(x_i)$, the constant spacing $\Delta x$, the number of points in the $x$-direction $N_x$ and $\overline{(\cdot)}$ denoting the ensemble average. The autocorrelation function is then normalised by $R^x_{uu}(0)$. The integral length scale is defined as $L^x_{uu} = \int_0^\infty R^x_{uu}$. For our case we define the upper integration boundary to the point, where the respective correlation function crosses a value of $1/e^2$. The integral length scales $L^x_{uu}$ and their heating-induced shortening is listed in table 3. We can make two observations: first, with increasing distance from the wall the structures grow larger and second, the heating leads to a slight shortening of the turbulent structures. As the temperature increase is highest close to the lower wall, we observe the strongest shortening in $L^x_{uu}$ there with a maximum value of −9.0% for $y^+ = 16.1$ corresponding to $y^+ = 24.2$ in the heated duct. For the transversal length scales of the streamwise velocity as well as the spanwise velocity we see a similar length scale reduction with the heating.

## 5. CONCLUSION

We investigated the three-dimensional flow field of a straight high aspect ratio cooling duct operated with water at a Reynolds-number of $110 \cdot 10^3$ with an asymmetric wall heating of $\Delta T = 40\,\mathrm{K}$ using a well-resolved LES. Good agreement, qualitatively and quantitatively, with experimental PTV as well as PIV measurements by [1] for the same configuration has been achieved for mean velocity and Reynolds stresses.

We analyzed the influence of the turbulence-induced secondary flow on the shape and growth of the developing temperature boundary layer along the duct. The pairs of counter-rotating vortices, which form in each of the duct corners, are relatively

Table 3: Integral length scales $L^x_{uu}$ and shortening $\Delta_{L^x_{uu}}$, where $L^x_{uu}$ is normalized by the hydraulic diameter $d_h$.

| $y^+$ | 16.1 | 30.1 | 60.5 | 120.6 | 627.0 |
|---|---|---|---|---|---|
| $L^x_{uu}\|_{per} \cdot 10^{-2}$ | 5.1 | 7.1 | 10.9 | 15.3 | 20.8 |
| $L^x_{uu}\|_{heat} \cdot 10^{-2}$ | 4.7 | 6.7 | 10.5 | 14.5 | 20.6 |
| $\Delta_{L^x_{uu}}$ | 9.0% | 6.3% | 4.2% | 5.2% | 1.2% |

weak (the maximum cross-flow velocity is $\approx 2\% u_b$ for our case), but they exhibit a significant effect on the temperature profile. The temperature rise signifies a drop in viscosity. Although the heating is moderate, we observed a significant weakening of the strength of the secondary flow along the duct length. The heated wall-normal velocity drops by up to −25% compared to the adiabatic case. As the secondary flow is turbulence-induced, we investigated the effects of the viscosity modulation on the near wall turbulence and the boundary layer profile. In agreement with [18] and [17], we observed a constant shift of the boundary layer velocity profile in the log-law region and a reduction of turbulence intensity in all directions. Using autocorrelation functions, we quantified the shortening of the turbulent length scales. By application of the barycentric anisotropy map to the Reynolds stress field, we showed that the turbulence anisotropy in the vicinity of the duct corners is reduced by the heating. The flow becomes more isotropic leading to a weaker production term for streamwise vorticity and in turn to a weakening of the secondary flow.

## ACKNOWLEDGEMENT

Financial support has been provided by the German Research Foundation (Deutsche Forschungsgemeinschaft – DFG) within the framework of the Sonderforschungsbereich Transregio 40, SFB-TRR40 (Technological foundations for the design of thermally and mechanically highly loaded components of future space transportation systems).

Computational resources have been provided by the Leibniz Supercomputing Centre Munich (LRZ).

The authors acknowledge helpful discussions with the people from the Institute of Fluid Mechanics, Technische Universität Braunschweig, who conduct the experimental investigation of the reference case; namely Henrik Rochlitz, Peter Scholz and Oliver Günther.

## REFERENCES

[1] Rochlitz, H., Scholz, P. and Fuchs, T. (2015). The flow field in a high aspect ratio cooling duct with and without one heated wall. *Experiments in Fluids*, **56**(12), 1–13.

[2] Baines, W. and Brundrett, E. (1964). The production and diffusion of vorticity in duct flow. *Journal of Fluid Mechanics*, **19**(03), 375.

[3] Gessner, F. and Jones, J. (1965). On some aspects of fully-developed turbulent flow in rectangular channels. *Journal of Fluid Mechanics*, **23**(4), 689–713.

[4] Launder, B.E. and Ying, W.M. (1972). Secondary flows in ducts of square cross-section. *Journal of Fluid Mechanics*, **54**(2), 289–295.

[5] Wardana, I.N.G., Ueda, T. and Mizomoto, M. (1994). Effect of strong wall heating on turbulence statistics of a channel flow. *Experiments in Fluids*, **18**(1), 87–94.

[6] Monty, J.P. (2005). *Developments In Smooth Wall Turbulent Duct Flows*. Ph.D. thesis, The University of Melbourne.

[7] Salinas-Vasquez, M. and Métais, O. (2002). Large-eddy simulation of the turbulent flow through a heated square duct. *Journal of Fluid Mechanics*, **453**, 201–238.

[8] Hébrard, J., Salinas-Vasquez, M. and Métais, O. (2005). Spatial development of turbulent flow within a heated duct. *Journal of Turbulence*, **6**, N8.

[9] Choi, H.S. and Park, T.S. (2013). The influence of streamwise vortices on turbulent heat transfer in rectangular ducts with various aspect ratios. *International Journal of Heat and Fluid Flow*, **40**, 1–14.

[10] Huser, A. and Biringen, S. (1993). Direct numerical simulation of turbulent flow in a square duct. *Journal of Fluid Mechanics*, **257**, 65–95.

[11] Vinuesa, R., Noorani, A., Lozano-Duran, A., El Khoury, G., Schlatter, P., Fischer, P.F. and Nagib, N.M. (2014). Aspect ratio effects in turbulent duct flows studied through direct numerical simulation. *Journal of Turbulence*, **15**(10), 677–706.

[12] IAPWS (2008). Release on the IAPWS Formulation 2008 for the Viscosity of Ordinary Water Substance. available from http://www.iapws.org.

[13] Gottlieb, S. and Shu, C. (1998). Total variation diminishing Runge-Kutta schemes. *Mathematics of Computation*, **67**(221), 73 – 85.

[14] Hickel, S., Adams, N.A. and Domaradzki, J.A. (2006). An adaptive local deconvolution method for implicit LES. *Journal of Computational Physics*, **213**(1), 413 – 436.

[15] Hickel, S., Egerer, C.P. and Larsson, J. (2014). Subgrid-scale modeling for implicit large eddy simulation of compressible flows and shock-turbulence interaction. *Physics of Fluids*, **26**(106101).

[16] Remmler, S. and Hickel, S. (2013). Spectral structure of stratified turbulence: Direct numerical simulations and predictions by large eddy simulation. *Theoretical and Computational Fluid Dynamics*, **27**(3-4), 319–336.

[17] Lee, J., Yoon Jung, S., Jin Sung, H. and Zaki, T.A. (2013). Effect of wall heating on turbulent boundary layers with temperature-dependent viscosity. *Journal of Fluid Mechanics*, **726**, 196–225.

[18] Zonta, F., Marchioli, C. and Soldati, A. (2012). Modulation of turbulence in forced convection by temperature-dependent viscosity. *Journal of Fluid Mechanics*, **697**, 150–174.

[19] Banerjee, S., Krahl, R., Durst, F. and Zenger, C. (2007). Presentation of anisotropy properties of turbulence, invariants versus eigenvalue approaches. *Journal of Turbulence*, **8**(32), 1–27.

[20] Pirozzoli, S., Grasso, F. and Gatski, T.B. (2004). Direct numerical simulation and analysis of a spatially evolving supersonic turbulent boundary layer at M = 2.25. *Physics of Fluids*, **16**(3), 530–545.